

GW190521: A dynamical capture of two black holes

Rossella Gamba¹, Matteo Breschi¹, Gregorio Carullo^{2,3}, Piero Rettegno^{4,5},
Simone Albanesi^{4,5}, Sebastiano Bernuzzi¹, and Alessandro Nagar^{5,6}

¹ *Theoretisch-Physikalisches Institut, Friedrich-Schiller-Universität Jena, 07743, Jena, Germany*

² *Dipartimento di Fisica “Enrico Fermi”, Università di Pisa, Pisa I-56127, Italy*

³ *INFN sezione di Pisa, Pisa I-56127, Italy*

⁴ *Dipartimento di Fisica, Università di Torino, via P. Giuria 1, 10125 Torino, Italy*

⁵ *INFN Sezione di Torino, Via P. Giuria 1, 10125 Torino, Italy and*

⁶ *Institut des Hautes Etudes Scientifiques, 91440 Bures-sur-Yvette, France*

(Dated: June 11, 2021)

We analyze the gravitational-wave signal GW190521 under the hypothesis that it was generated by the merger of two nonspinning black holes on hyperbolic orbits. The best configuration matching the data corresponds to two black holes of source frame masses of $81^{+62}_{-25}M_{\odot}$ and $52^{+32}_{-32}M_{\odot}$ undergoing two encounters and then merging into an intermediate-mass black hole. Under the hyperbolic merger hypothesis, we find an increase of one unit in the recovered signal-to-noise ratio and a 14 e-fold increase in the maximum likelihood value compared to a quasi-circular merger with precessing spins. We conclude that our results support the first gravitational-wave detection from the dynamical capture of two stellar-mass black holes.

Introduction.— The gravitational-wave (GW) transient GW190521, detected by the LIGO-Virgo network [1, 2], is compatible with the quasi-circular merger of two heavy ($m_1 \simeq 85M_{\odot}$, $m_2 \simeq 66M_{\odot}$) black holes (BHs) resulting in an $\simeq 150M_{\odot}$ intermediate-mass BH (IMBH) [3, 4]. The estimated BH component masses fall in a “forbidden range” $\simeq 65 - 120M_{\odot}$ for BHs formed directly from stellar collapse, and challenge standard scenarios on BHs formation [4–11]. The short duration (~ 0.1 s) of GW190521 and the absence of a premerger signal, identified also by unmodeled (or weakly modeled) analyses [1], are critical aspects for the choice of waveform templates in matched filtering analyses and thus for the interpretation of the source. For example, under the hypothesis of a quasi-circular merger, matching the signal morphology requires fairly large in-plane components of the individual BH spins and results in a (weak) statistical evidence for orbital-plane precession. High orbital eccentricities (notably, head-on collisions) are also compatible with the burst-like morphology of GW190521 [12], although best-matching eccentric merger waveforms still require spin precession [13, 14]. Other proposed interpretations involve a boson-star merger [15], a high-mass black hole-disk system [16] or an intermediate mass ratio inspiral [17] (see also [18]), and indicate that the origin of GW190521 is still unsettled.

In this *Letter* we interpret GW190521 within the scenario of a binary black hole (BBH) dynamical capture and demonstrate that this hypothesis is more plausible than that of a quasi-circular merger. Dynamical captures have a phenomenology radically different from quasi-circular mergers [19–21]. The close passage and capture of the two objects in hyperbolic orbits naturally accounts for the short-duration, burst-like waveform morphology of GW190521 even in the absence of spins. Moreover, possible explanations of the high component

masses rely on second-generation BHs, stellar mergers in young star clusters and BH mergers in active galactic nuclei disks, e.g. [5–11, 22, 23], for which dynamical captures are possible. While no observational evidence for GWs from dynamical captures existed prior to our work, such events are not incompatible with the current detection rates [24].

Phenomenology of hyperbolic mergers.— A significant progress in constructing waveform templates for black hole binaries on hyperbolic orbits has been recently made within the effective-one-body (EOB) approach [25–27]. The EOB method [28–32] is a powerful analytical formalism that suitably resums post-Newtonian (PN) results [33, 34] (obtained via a perturbative expansion of Einstein’s field equations in powers of the inverse of the speed of light c^{-1}) in the weak-field, small-velocity regime and makes them reliable and predictive also when the field is strong and velocities are comparable to c , i.e. up to merger and ringdown. The framework introduced in Ref. [25–27] fully accounts for the dynamical capture phenomenology and delivers complete waveform templates from hyperbolic mergers. The method is a generalization of the quasi-circular, spin-aligned waveform model **TEOBResumS** [35, 36] to deal with arbitrarily eccentric orbits, from eccentric inspirals to hyperbolic mergers. For simplicity, however, the EOB analytical waveform for hyperbolic mergers does not contain next-to-quasi-circular corrections informed by numerical relativity (NR) simulations and it is completed by a NR-informed quasi-circular ringdown [36]. The reason for this choice is that, although some NR simulations are available [19, 20, 37–40], a systematic coverage of the BBH parameter space for hyperbolic orbits is currently missing.

The analytical model generates waveforms and scattering angles that are faithful to NR BBH simulations of eccentric and scattering orbits [25–27, 40]. The reliability

of this EOB approach in describing dynamical captures is further tested in the test-mass limit of a body captured by a Schwarzschild BH using the waveforms computed numerically using black hole perturbation theory [41, 42]. These results, together with a comparisons with new NR data, will be reported in detail elsewhere. Although the model includes aligned spins and subdominant multipoles in the waveforms, here we focus on nonspinning BBHs and use only the dominant $\ell = m = 2$ quadrupole mode.

The EOB relative motion is described using mass-reduced phase-space variables $(r, \varphi, p_\varphi, p_{r_*})$, related to the physical ones by [in geometric units $G = c = 1$] $r = R/M$ (relative separation), φ (orbital phase), $p_{r_*} \equiv P_{R_*}/\mu$ (radial momentum), $p_\varphi \equiv P_\varphi/(\mu M)$ (angular momentum) and $t \equiv T/M$ (time), where $\mu \equiv m_1 m_2 / M$ and $M \equiv m_1 + m_2$. The EOB Hamiltonian is $\hat{H} \equiv H/\mu \equiv \nu^{-1} \sqrt{1 + 2\nu(\hat{H}_{\text{eff}} - 1)}$, with $\nu \equiv \mu/M$ and \hat{H}_{eff} is the effective Hamiltonian of Ref. [25, 26, 36, 43]. For nonspinning binaries, the configuration space can be characterized by the mass ratio $q = m_1/m_2 \geq 1$, the initial energy E_0/M and the initial reduced orbital angular momentum p_φ^0 [26]. Similarly to the motion of a test particle moving around a Schwarzschild BH, the EOB behavior of a hyperbolic encounter is characterized by the EOB potential energy $E_{\text{EOB}} \equiv M \sqrt{1 + 2\nu(\hat{W}_{\text{eff}} - 1)}$, where $\hat{W}_{\text{eff}} = \sqrt{A(r)(1 + p_\varphi^2/r^2)}$ is the effective potential energy. Here, $A(r) \equiv P_5^1[A_{5\text{PN}}(r)]$ is the Padé resummed EOB radial potential, where $A_{5\text{PN}}(r) = 1 - 2/r + \nu a(\nu, r)$ indicates its Taylor-expanded form, that reduces to the Schwarzschild case in the test-particle limit, $\nu = 0$. The function $a(\nu, r)$ incorporates high-order corrections up to 5PN and it is additionally informed by NR simulations [25, 26, 36, 44]. The solution $\partial_r W_{\text{eff}} = \partial_r^2 W_{\text{eff}} = 0$ defines last stable orbit (LSO) parameters $(r_{\text{LSO}}, p_\varphi^{\text{LSO}})$. When $p_\varphi > p_\varphi^{\text{LSO}}$, W_{eff} has both a maximum and a minimum and, depending on E_0/M , bound as well as unbound configurations are present. In the absence of radiation reaction, unbound configurations are defined by the condition $E_0/M > 1$. We define $E_{\text{min}}/M \equiv \nu \hat{H}(r_0, q, p_\varphi, p_r = 0)$ the energy corresponding to the initial separation and $E_{\text{max}}/M = \max_r [\nu \hat{H}(r, q, p_\varphi, p_r = 0)]$. For a given p_φ , the values $(E_{\text{max}}, E_{\text{min}})$ correspond respectively to unstable and stable circular orbits, analogously to Schwarzschild geodesics. When $E_0 > E_{\text{max}}$ the objects fall directly onto each other without forming metastable configurations (e.g., for head-on collisions, corresponding to $p_\varphi = 0$). When $1 < E_0/M \leq E_{\text{max}}/M$, the phenomenology changes from direct plunge, to on up to many close passages before merger, to zoom-whirl behavior or even scattering [37, 39, 40].

In the presence of radiation reaction, the qualitative picture remains unchanged (as also observed in NR simulations [20]), although the threshold between the two

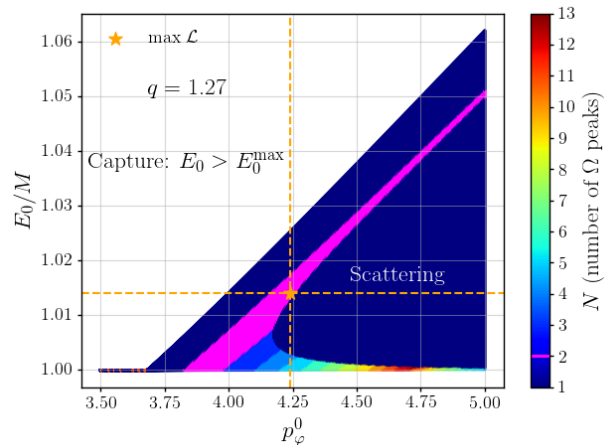


FIG. 1. Parameter space for nonspinning hyperbolic encounters predicted using the **TEOBResumS** EOB model and fixing $q \equiv m_1/m_2 = 1.27$. Here (p_φ^0, E_0) are the EOB initial angular momentum and energy, while E_0^{max} is the value corresponding to unstable circular orbit. For $E_0 < E_0^{\text{max}}$, each color labels the number of peaks (i.e. of periastron passages) N of the EOB orbital frequency Ω . The orange star labels the maximum likelihood values $(\bar{p}_\varphi^0, \bar{E}_0)$ corresponding to the *constrained* analysis, see Table I.

qualitative behaviors is not simply set by E_{max} , but it is also affected by GW losses. The latter are taken into account through the azimuthal and radial radiation reaction forces $(\mathcal{F}_\varphi, \mathcal{F}_r)$ described in detail in [25, 26]. The dynamics of each configuration can be characterized by counting the number of peaks of the orbital frequency $\Omega(t) \equiv \dot{\varphi}$, each peak corresponding to a periastron passage [26]. Figure 1 illustrates the $(E_0/M, p_\varphi^0)$ parameter space, defined using the peaks of $\Omega(t)$, of a nonspinning binary with $q = 1.27$, corresponding to the best-matching mass ratio for the GW190521 analysis. The different colors indicate the number of encounters. Although the two dark blue areas, above and below the magenta zone, possess a single peak in Ω , they correspond to different phenomenologies. The dark-blue region *above* the magenta area corresponds to a direct capture scenario, that eventually leads to a ringdown phase. The dark-blue region *below* the magenta area corresponds to a scattering scenario. The single-burst waveform morphology is obtained for $(E_0/M, p_\varphi^0)$ within the blue capture region as well as the upper boundary of the magenta region, until a distinct second burst of GWs does not appear before the one corresponding to the final merger. The single burst phenomenology also occurs in the white region $E_0 > E_{\text{max}}$ in Fig. 1, where there exist systems with low values of p_φ^0 and large initial energies. Waveforms emitted by such binaries are dominated by the ringdown.

GW190521 analysis.— The publicly released GW190521 data are analyzed around time

TABLE I. Source parameters of GW190521, m_1 (m_2) is the mass of the heavier (lighter) object, M_{source} is the total mass in the frame of the source, χ_{eff} is the effective spin along the orbital angular momentum, while χ_{p} is the effective precessing spin [3]. The second and third columns report our new results, obtained with the hyperbolic capture model of [26] with the two different prior choices on the energy. The fourth and the fifth columns report the results obtained in this work with the quasi-circular model **NRSur7dq4**. For reference, the remaining columns report results of Refs. [3, 13, 14]. We employ the standard cosmology of [45] to compute source frame masses. Median values and 90% credible intervals are quoted and natural logarithms are reported.

Reference	This paper				LVC [3]	Ref. [13]	Ref. [14]
Waveform	TEOBResumS [25, 26]	TEOBResumS [25, 26]	NRSur7dq4 [46]	NRSur7dq4 [46]	NRSur7dq4 [46]	NR	SEOBNRE [47]
E_0 prior	Unconstrained (UE ₀)		Constrained (CE ₀)		–	–	–
Multipoles	$(\ell, m) = (2, 2)$	$(\ell, m) = (2, 2)$	$(\ell, m) = (2, 2)$	$\ell \leq 4$	$\ell \leq 4$	–	–
$m_1 [M_\odot]$	85^{+88}_{-22}	81^{+62}_{-25}	120^{+42}_{-34}	83^{+20}_{-14}	85^{+21}_{-14}	102^{+7}_{-11}	92^{+26}_{-16}
$m_2 [M_\odot]$	59^{+18}_{-37}	52^{+32}_{-32}	49^{+29}_{-22}	63^{+15}_{-15}	66^{+17}_{-18}	102^{+7}_{-11}	69^{+18}_{-19}
$M_{\text{source}} [M_\odot]$	151^{+73}_{-51}	130^{+75}_{-43}	171^{+27}_{-25}	146^{+24}_{-17}	150^{+29}_{-17}	–	–
$m_2/m_1 \leq 1$	$0.69^{+0.27}_{-0.52}$	$0.63^{+0.31}_{-0.43}$	$0.43^{+0.43}_{-0.25}$	$0.77^{+0.20}_{-0.28}$	$0.79^{+0.19}_{-0.29}$	–	–
χ_{eff}	–	–	$0.02^{+0.24}_{-0.27}$	$0.09^{+0.38}_{-0.25}$	$0.08^{+0.27}_{-0.36}$	0	$0.0^{+0.2}_{-0.2}$
χ_{p}	–	–	$0.78^{+0.17}_{-0.37}$	$0.66^{+0.27}_{-0.36}$	$0.68^{+0.25}_{-0.37}$	0.7	–
e	–	–	–	–	–	0.67	0.11 ^a
E^0/M	$1.014^{+0.009}_{-0.012}$	$1.014^{+0.010}_{-0.012}$	–	–	–	–	–
p_φ^0	$4.18^{+0.50}_{-0.62}$	$4.24^{+0.57}_{-0.37}$	–	–	–	–	–
SNR	15.2	15.4	14.1	14.2	14.7	–	–
$\log(\mathcal{L})_{\text{max}}$	123.2	123.0	109.2	107.4	–	–	–
$\log \mathcal{B}_{\text{noise}}^{\text{signal}}$	84.00 ± 0.18	83.30 ± 0.18	74.52 ± 0.16	74.76 ± 0.15	–	–	–

^a Lower limit at 10 Hz.

$t_{\text{GPS}} = 1242442968$, with an 8 s time-window and in the range of frequencies [11, 512] Hz using the **bajes** pipeline [48]. We employ the power-spectral-density estimate and calibration envelopes publicly available from the GW Open Science Center [49]. The Bayesian analysis uses the **dynesty** sampler [50] with 2048 live points. We use a uniform prior in the mass components (m_1, m_2) exploring the ranges of chirp mass $\mathcal{M}_c \in [30, 200] M_\odot$ and mass ratio $q \in [1, 8]$. The luminosity distance is sampled assuming a volumetric prior in the range [1, 10] Gpc. We analytically marginalize over the coalescence phase, and sample the coalescence time in $t_s \in [-2, 2]$ s with respect to the central GPS time.

The key quantities to sample the configuration space of hyperbolic mergers are $(E_0/M, p_\varphi^0)$. The initial angular momentum is uniformly sampled within $p_\varphi^0 \in [3.5, 5]$, and further imposing $p_\varphi^0 \geq p_\varphi^{\text{LSO}}$ for any q . The initial energy is uniformly sampled in the interval $E_0/M \in [1.002, 1.025]$ but with two different additional constraints that result in two different prior choices: (UE₀) *Unconstrained prior*: $E_0 \geq E_{\text{min}}$; (CE₀) *Constrained prior*: $E_{\text{min}} \leq E_0 \leq E_{\text{max}}$. The UE₀ prior spans a larger portion of the parameter space, notably including direct capture, although the dynamic remains far from the head-on collision case. The CE₀ prior is contained in the first, and restricts the parameter space to systems closer to stable configurations, for which the

orbital dynamics substantially contributes to the waveform and the ringdown description is expected to be more accurate.

The results of the analysis corresponding to the UE₀ and CE₀ priors are summarized in the second and third columns of Table I respectively. The consistency of the two measurements confirms the robustness of our modeling choices. Focusing on global fitting quantities we find, respectively for the UE₀ (CE₀) priors, maximum likelihood values $\log(\mathcal{L})_{\text{max}} = 123.2$ (123.0), and Bayesian evidences $\log \mathcal{B}_{\text{noise}}^{\text{signal}} = 84.0 \pm 0.18$ (83.3 ± 0.18), while the recovered signal-to-noise ratio (SNR) is equal to 15.2 (15.4). Employing the standard cosmology of Ref. [45], we find component masses in the source frame $(m_1, m_2) = (85^{+88}_{-22}, 59^{+18}_{-37}) M_\odot$ for the UE₀ case and $(m_1, m_2) = (81^{+62}_{-25}, 52^{+32}_{-32}) M_\odot$ in the CE₀ case. Figure 2 illustrates the (E_0, p_φ^0) parameter space selected by the analysis, with colors highlighting configurations with different number of encounters N . The figure shows that, despite GW190521 consisting of a single GW burst around the analyzed time, many of the configurations selected, and in particular the most probable ones, corresponds to two encounters.

The phenomenology corresponding to the set of maximum likelihood parameters selected by the analysis are shown in Fig. 3. The EOB relative trajectory (top panel) is complemented by the corresponding waveform templates projected onto the three detectors and compared

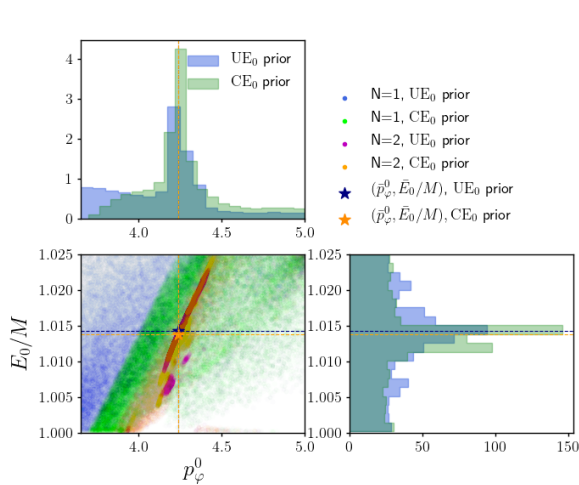


FIG. 2. Marginalized two-dimensional posterior distributions of the initial energy E_0 and initial angular momentum p_φ^0 for the constrained (CE_0) and unconstrained (UE_0) energy prior choices. The colors highlight the different waveform phenomenologies, with $N = 1$ (blue and green) or $N = 2$ (magenta and orange) peaks in the orbital frequency. The maximum likelihood values $(\bar{p}_\varphi^0, \bar{E}_0)$ are highlighted with red (UE_0 prior) and dark-orange (CE_0 prior) stars.

to the whitened LIGO-Virgo data around the time of GW190521. Thicker lines highlight the last part of the dynamics, which exactly covers the portion of the signal displayed in the bottom panel. The magnitude of the first GW burst predicted by the EOB analysis (not shown in the plot) is comparable to the detector noise and would occur outside the analysis window. However, we find that such first burst is not a robust feature across samples, occurring at different times and smaller amplitudes for different points and not occurring at all for others (see Fig. 2). Given this consideration and the small amplitude of such first burst, we do not expect an extension of the analysis segment to impact our main conclusions.

In order to reduce systematics when comparing the hyperbolic capture model to the quasi-circular model, we repeat the quasi-circular analysis with the precessing surrogate model `NRSur7dq4` [46] by using the `bajes` pipeline [48]. The prior distributions for the mass parameters and the extrinsic parameters are identical to the ones used in the hyperbolic capture analysis with `TEOBResumS`, while the prior on the spin components is chosen to be uniform in the spin magnitudes and isotropic in the angles [3]. When including higher modes, we disable phase marginalisation and to achieve a fair comparison with the other approximants, in Table I we quote maximum likelihood and SNR values obtained from the full unmarginalised posterior. The quasi-circular precessing analyses with `bajes` are in close agreement (both on parameter posterior distributions and SNR estimates)

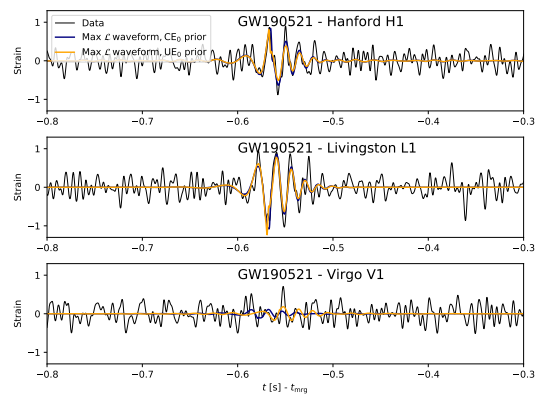
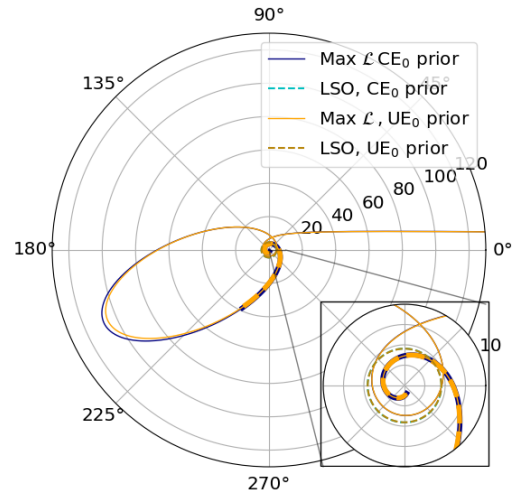


FIG. 3. Maximum likelihood configurations with the two different energy priors, UE_0 (orange) and CE_0 (blue). Top: the (r, φ) EOB relative orbit. Bottom: the waveform templates projected onto the three detectors compared to the whitened LIGO-Virgo data around the time of GW190521. The most probable last stable orbits (LSO) are highlighted with gold (UE_0 prior) and cyan (CE_0 prior) dashed lines and are located, respectively, at $\bar{r}_{\text{LSO}} = 4.54$ and $\bar{r}_{\text{LSO}} = 4.52$. Corresponding mass ratios are $\bar{q} = 1.04$ and $\bar{q} = 1.27$. The inset highlights the first close encounter, that is then followed by a highly eccentric orbit that eventually ends up with a plunge and merger phase. The part of the trajectory from $\sim (t_{\text{GPS}} - 0.8 \text{ s})$ to merger, which contributes to the second GW burst, is highlighted with thicker lines in the plot. Note that the GW bursts corresponding to the first encounter occur $\sim 4 \text{ s}$ before the GW190521 time, their magnitude is comparable to the detector noise and are outside the segment of data analyzed.

with those of Ref. [3], as reported in Table I, confirming the reliability of the adopted sampler.

Discussion.— Despite the different hypotheses on the coalescence process, our results on the component masses are in good agreement with the ones obtained from a quasi-circular model. This confirms that an IMBH is

formed at the end of the coalescence. The consistency on the total mass is not surprising, given that the dominant contribution to this parameter comes from the determination of the ringdown frequency [3]. However, the dynamical capture model is able to fit GW data significantly better than the quasi-circular scenario, with a 14 e-fold increase in the maximum likelihood value. This result is even more remarkable given that the non-circular model does not possess spin degrees of freedom, hence having four less parameters than the quasi-circular model. Also, under the dynamical capture assumption, we obtain a SNR $\rho = 15.4$, larger by a factor of unity with respect to the value obtained using quasi-circular waveforms. The fit improvement registered by these two indicators is confirmed by the Bayesian evidences, keeping into account the full correlation structure of the parameter space, which imply odds of $\sim 24300:1$ in favor of the dynamical encounter scenario against the quasi-circular scenario. It should however be noted that this last number can receive a penalty due to the larger dimensionality of the quasi-circular model which is not phase marginalized and includes precessing spins degrees of freedom, only weakly measurable. All these results constitute robust data-driven indicators that the interpretation of GW190521 within the dynamical capture scenario is more plausible than quasi-circular spin-precessing merger [1, 18]. As further check of our results, we performed injections of dynamical-capture signals and recover them with precessing quasi-circular templates [51]. Our findings are consistent with the fact that burst-like waveforms from highly eccentric or head-on BBH collision may be confused with mildly precessing quasi-circular binaries [12]. Regarding other possible scenarios, a quantitative comparison is currently not possible since they have not been analyzed with full Bayesian studies and/or complete waveform templates [13, 15, 16].

While our analysis selects a two-encounters merger as best-fitting capture scenario (Fig. 3), the orbital dynamics of these encounters is rather sensitive to changes in both the conservative and nonconservative part of the dynamics [26], as also evident from Fig. 1.

Going beyond the conservative assumptions behind our analysis, future work will explore the impact of spin and of higher waveform multipoles, as well as consider systematic comparisons between our (improved [27]) EOB model and NR simulations. The inclusion of additional, physically motivated, degrees of freedom in the model (e.g., BH spins) is expected to strengthen the interpretation of GW190521 as the first observed dynamical capture of two black holes.

Acknowledgments. — We are grateful to T. Damour, J. A. Font and T. Andrade for discussions. R.G. acknowledges support from the Deutsche Forschungsgemeinschaft (DFG) under Grant No. 406116891 within the Research Training Group RTG 2522/1. M.B., S.B. acknowledge support by the EU H2020 under ERC Start-

ing Grant, no. BinGraSp-714626. M.B. acknowledges partial support from the Deutsche Forschungsgemeinschaft (DFG) under Grant No. 406116891 within the Research Training Group RTG 2522/1. The computational experiments were performed on resources of Friedrich Schiller University Jena supported in part by DFG grants INST 275/334-1 FUGG and INST 275/363-1 FUGG, EU H2020 BinGraSp-714626, and on the Tullio sever at INFN Turin. We thank E. Ferrari for speed-up coding work on Tullio.

The waveform model used in this work, `TEOBResumS`, is publicly available at: https://bitbucket.org/eob_ihes/teobresums/ and results presented in this paper have been obtained with the version tagged `eccentric.v0.a6c_c3.circularized`. This research has made use of data, software and/or web tools obtained from the Gravitational Wave Open Science Center (<https://www.gw-openscience.org>), a service of LIGO Laboratory, the LIGO Scientific Collaboration and the Virgo Collaboration. LIGO is funded by the U.S. National Science Foundation. Virgo is funded by the French Centre National de Recherche Scientifique (CNRS), the Italian Istituto Nazionale della Fisica Nucleare (INFN) and the Dutch Nikhef, with contributions by Polish and Hungarian institutes.

-
- [1] J. Aasi *et al.* (LIGO Scientific), *Class. Quant. Grav.* **32**, 074001 (2015), arXiv:1411.4547 [gr-qc].
 - [2] F. Acernese *et al.* (VIRGO), *Class. Quant. Grav.* **32**, 024001 (2015), arXiv:1408.3978 [gr-qc].
 - [3] R. Abbott *et al.* (LIGO Scientific, Virgo), *Phys. Rev. Lett.* **125**, 101102 (2020), arXiv:2009.01075 [gr-qc].
 - [4] R. Abbott *et al.* (LIGO Scientific, Virgo), *Astrophys. J. Lett.* **900**, L13 (2020), arXiv:2009.01190 [astro-ph.HE].
 - [5] R. Abbott *et al.* (LIGO Scientific, Virgo), (2020), arXiv:2010.14533 [astro-ph.HE].
 - [6] E. González, K. Kremer, S. Chatterjee, G. Fragione, C. L. Rodriguez, N. C. Weatherford, C. S. Ye, and F. A. Rasio, *Astrophys. J. Lett.* **908**, L29 (2021), arXiv:2012.10497 [astro-ph.HE].
 - [7] K. Belczynski, *Astrophys. J. Lett.* **905**, L15 (2020), arXiv:2009.13526 [astro-ph.HE].
 - [8] M. Mapelli *et al.*, (2021), 10.1093/mnras/stab1334, arXiv:2103.05016 [astro-ph.HE].
 - [9] M. A. Sedda, F. P. Rizzuto, T. Naab, J. Ostriker, M. Giersz, and R. Spurzem, (2021), arXiv:2105.07003 [astro-ph.GA].
 - [10] H. Tagawa, Z. Haiman, I. Bartos, B. Kocsis, and K. Omukai, (2021), arXiv:2104.09510 [astro-ph.HE].
 - [11] M. Dall’Amico, M. Mapelli, U. N. Di Carlo, Y. Bouffanais, S. Rastello, F. Santoliquido, A. Ballone, and M. A. Sedda, (2021), arXiv:2105.12757 [astro-ph.HE].
 - [12] J. Calderón Bustillo, N. Sanchis-Gual, A. Torres-FornE9, and J. A. Font, (2020), arXiv:2009.01066 [gr-qc].
 - [13] V. Gayathri, J. Healy, J. Lange, B. O’Brien, M. Szczepanczyk, I. Bartos, M. Campanelli, S. Klimenko, C. Lousto, and R. O’Shaughnessy, (2020),

- arXiv:2009.05461 [astro-ph.HE].
- [14] I. M. Romero-Shaw, P. D. Lasky, E. Thrane, and J. C. Bustillo, (2020), arXiv:2009.04771 [astro-ph.HE].
- [15] J. Calderón Bustillo, N. Sanchis-Gual, A. Torres-Forné, J. A. Font, A. Vajpeyi, R. Smith, C. Herdeiro, E. Radu, and S. H. W. Leong, (2020), arXiv:2009.05376 [gr-qc].
- [16] M. Shibata, K. Kiuchi, S. Fujibayashi, and Y. Sekiguchi, Phys. Rev. D **103**, 063037 (2021), arXiv:2101.05440 [astro-ph.HE].
- [17] A. H. Nitz and C. D. Capano, Astrophys. J. Lett. **907**, L9 (2021), arXiv:2010.12558 [astro-ph.HE].
- [18] H. Estellés *et al.*, (2021), arXiv:2105.06360 [gr-qc].
- [19] W. E. East, S. T. McWilliams, J. Levin, and F. Pretorius, Phys. Rev. **D87**, 043004 (2013), arXiv:1212.0837 [gr-qc].
- [20] R. Gold and B. Brügmann, Phys. Rev. **D88**, 064051 (2013), arXiv:1209.4085 [gr-qc].
- [21] N. Loutrel, (2020), arXiv:2009.11332 [gr-qc].
- [22] A. Rasskazov and B. Kocsis, Astrophys. J. **881**, 20 (2019), arXiv:1902.03242 [astro-ph.HE].
- [23] H. Tagawa, Z. Haiman, and B. Kocsis, Astrophys. J. **898**, 25 (2020), arXiv:1912.08218 [astro-ph.GA].
- [24] S. Mukherjee, S. Mitra, and S. Chatterjee, (2020), arXiv:2010.00916 [gr-qc].
- [25] D. Chiaromello and A. Nagar, Phys. Rev. D **101**, 101501 (2020), arXiv:2001.11736 [gr-qc].
- [26] A. Nagar, P. Rettegno, R. Gamba, and S. Bernuzzi, Phys. Rev. D **103**, 064013 (2021), arXiv:2009.12857 [gr-qc].
- [27] A. Nagar, A. Bonino, and P. Rettegno, (2021), arXiv:2101.08624 [gr-qc].
- [28] A. Buonanno and T. Damour, Phys. Rev. **D59**, 084006 (1999), arXiv:gr-qc/9811091.
- [29] A. Buonanno and T. Damour, Phys. Rev. **D62**, 064015 (2000), arXiv:gr-qc/0001013.
- [30] T. Damour, P. Jaranowski, and G. Schaefer, Phys. Rev. **D62**, 084011 (2000), arXiv:gr-qc/0005034 [gr-qc].
- [31] T. Damour, Phys. Rev. **D64**, 124013 (2001), arXiv:gr-qc/0103018.
- [32] T. Damour, P. Jaranowski, and G. Schäfer, Phys. Rev. **D91**, 084024 (2015), arXiv:1502.07245 [gr-qc].
- [33] L. Blanchet, Living Rev. Relativity **17**, 2 (2014), arXiv:1310.1528 [gr-qc].
- [34] G. Schaefer and P. Jaranowski, Living Rev. Rel. **21**, 7 (2018), arXiv:1805.07240 [gr-qc].
- [35] A. Nagar *et al.*, Phys. Rev. **D98**, 104052 (2018), arXiv:1806.01772 [gr-qc].
- [36] A. Nagar, G. Riemenschneider, G. Pratten, P. Rettegno, and F. Messina, (2020), arXiv:2001.09082 [gr-qc].
- [37] F. Pretorius and D. Khurana, Class.Quant.Grav. **24**, S83 (2007), arXiv:gr-qc/0702084 [GR-QC].
- [38] J. Healy, J. Levin, and D. Shoemaker, Phys.Rev.Lett. **103**, 131101 (2009), arXiv:0907.0671 [gr-qc].
- [39] U. Sperhake, V. Cardoso, F. Pretorius, E. Berti, T. Hinderer, *et al.*, Phys.Rev.Lett. **103**, 131102 (2009), arXiv:0907.1252 [gr-qc].
- [40] T. Damour, F. Guercilena, I. Hinder, S. Hopper, A. Nagar, *et al.*, (2014), arXiv:1402.7307 [gr-qc].
- [41] E. Harms, S. Bernuzzi, A. Nagar, and A. Zenginoglu, Class.Quant.Grav. **31**, 245004 (2014), arXiv:1406.5983 [gr-qc].
- [42] S. Albanesi, A. Nagar, and S. Bernuzzi, (2021), arXiv:2104.10559 [gr-qc].
- [43] G. Riemenschneider, P. Rettegno, M. Breschi, A. Albertini, R. Gamba, S. Bernuzzi, and A. Nagar, (2021), arXiv:2104.07533 [gr-qc].
- [44] A. Nagar, G. Pratten, G. Riemenschneider, and R. Gamba, (2019), arXiv:1904.09550 [gr-qc].
- [45] N. Aghanim *et al.* (Planck), Astron. Astrophys. **641**, A6 (2020), arXiv:1807.06209 [astro-ph.CO].
- [46] V. Varma, S. E. Field, M. A. Scheel, J. Blackman, D. Gerosa, L. C. Stein, L. E. Kidder, and H. P. Pfeiffer, Phys. Rev. Research. **1**, 033015 (2019), arXiv:1905.09300 [gr-qc].
- [47] Z. Cao and W.-B. Han, Phys. Rev. **D96**, 044028 (2017), arXiv:1708.00166 [gr-qc].
- [48] M. Breschi, R. Gamba, and S. Bernuzzi, preprint (ArXiv:2102.00017) (2021), arXiv:2102.00017 [gr-qc].
- [49] R. Abbott *et al.* (LIGO Scientific, Virgo), (2019), arXiv:1912.11716 [gr-qc].
- [50] J. S. Speagle, Monthly Notices of the Royal Astronomical Society **493**, 3132?3158 (2020).
- [51] R. Gamba *et al.*, (2021).